Additive Manufacturing 25 (2019) 421–429

Contents lists available at ScienceDirect

Additive Manufacturing

journal homepage: www.elsevier.com/locate/addma

Mechanical vibration bandgaps in surface-based lattices

Waiel Elmadih[a,*], Wahyudin P. Syam[a], Ian Maskery[b], Dimitrios Chronopoulos[c], Richard Leach[a]

[a] Manufacturing Metrology Team, Faculty of Engineering, University of Nottingham, UK
[b] Centre for Additive Manufacturing, Faculty of Engineering, University of Nottingham, UK
[c] Institute for Aerospace Technology & The Composites Group, University of Nottingham, UK

ARTICLE INFO

Keywords:
Lattice structures
Phononic materials
Mechanical bandgaps
Design for additive manufacturing

ABSTRACT

In this paper, the phonon dispersion curves of several surface-based lattices are examined, and their energy transmission spectra, along with the corresponding bandgaps are identified. We demonstrate that these bandgaps may be controlled, or tuned, through the choice of cell type, cell size and volume fraction. Our results include two findings of high relevance to the designers of lattice structures: (i) network and matrix phase gyroid lattice structures develop bandgaps below 15 kHz while network diamond and matrix diamond lattices do not, and (ii) the bandwidth of a bandgap in the network phase gyroid lattice can be tuned by adjusting its volume fraction and cell size.

1. Introduction

Vibration can be a significant issue in precision engineering, contributing to measurement uncertainties and limiting manufacturing precision. When the amplitude is high enough, vibration can cause physical damage, especially when the frequency of the incident wave is at or close to the natural frequency of the mechanical system in question. Conventional practice is to design the mechanical system to have a natural frequency much greater than or lower than the frequencies of the input waves [1–3]. Using the conventional practice, our previous work has shown that additively manufactured (AM) lattice structures can be used for vibration isolation in one degree of freedom (DOF) by designing the lattice to have a resonant frequency lower than a particular frequency of interest [4]. Further to this, Wang et al. showed how topology optimisation and density grading could be implemented with AM lattice structures to provide isolation in a selected frequency region [5].

One of the drawbacks of the conventional vibration isolation practice is that it does not guarantee complete elimination of vibration in the frequency of interest. An alternative approach is to design structures that exhibit phononic bandgaps. AM gives us the freedom to design and manufacture these phononic bandgap structures and, more importantly, to tailor the structural parameters and to tune the properties for specific applications.

A phononic bandgap is a range of frequencies in which the propagation of elastic waves is prohibited by Bragg scattering. The bandgap is caused by the destructive interference of reflected waves of certain frequencies as they propagate through a periodic medium [6,7]. Bandgap structures have been reported for use in a range of applications. Recent examples relevant to the aerospace sector include the work of Ampatzidis et al. [8], who presented a bandgap structure to act as an acoustic isolator. Design parameters of bandgaps have been studied by Richards and Pines [9], who used the principles of stop-band/pass-band for the reduction of vibration in a mesh of mechanical gears. Sigmund and Jensus presented a design of a waveguide [10], Diaz et al. designed a bandgap structure using non-structural masses as design parameters to control features in the dispersion curves [11], Lucklum et al. [12] presented additively manufactured lattice structures on the millimetre-scale, Kruisova et al. [13] tested bandgaps in ceramic lattices, and Wormser et al. [14] presented an approach for maximisation of bandgaps through gradient optimisation. In addition, Maurin et al. [15] presented a statistical analysis of the issues associated with restricting the detection of bandgaps to the contour of the irreducible Brillouin zone (IBZ) instead of the full IBZ. They have reported that restricting the detection to only the contour of the IBZ provides accurate results when the lattice is of high structural symmetry.

Recent studies that have investigated cellular structures for use as bandgap structures include the work of Ruzzene et al. [16], who studied grid cellular structures and presented a method for the guidance of waves, Abueidda et al. [17], showed that primitive cell, IWP and Neovious triply periodic minimal surface (TPMS) lattices can develop three-dimensional (3D) bandgaps and presented a method for controlling them, Matlack et al. [18], presented structures that provide vibration absorption at frequencies as low as 3 kHz–4 kHz using lattices of

* Corresponding author.
E-mail address: Waiel.Elmadih@nottingham.ac.uk (W. Elmadih).

https://doi.org/10.1016/j.addma.2018.11.011
Received 25 April 2018; Received in revised form 7 November 2018; Accepted 9 November 2018
Available online 13 November 2018

different stiffness [18], and Li et al. [19], examined the dispersion curves of two-dimensional (2D) phononic crystals using a finite element method.

The mechanical properties of TPMS lattices can be modified by controlling their volume fraction [20]. TPMS lattices have complex morphologies making their fabrication by conventional manufacturing methods challenging, if not impossible. AM enables the fabrication of TPMS lattices for a range of applications, but the literature to date has focussed mainly on their load-bearing capability [20–22]. There exists a wide range of TPMS lattice cell types [20,22,23]. In this paper, four types of TPMS structures are considered for the development of 1D phononic bandgaps under 15 kHz, which represents part of the acoustic frequency range. The nature of the bandgaps presented in this work is realised by the tessellations of the unit cells along one single direction which form a beam-like lattice, hence the name '1D'. However, the dispersion curves, from which the bandgaps will be extracted, rely on three degrees of freedom of the nodes associated with the 3D unit cell model; this ensures that the dispersion curves pick up the transverse waves as well as the longitudinal waves in the structure. The TPMS lattices examined in this paper are the network gyroid, network diamond, matrix gyroid and matrix diamond. These lattice types have proved to provide high resistance to compressive failure [23,24], have higher manufacturability than other strut-based lattices due to less stress concentration during AM [24,25], and provide high structural stiffness for use in different applications [26]. To the authors' knowledge the phononic behaviour of the considered lattices has not been studied before.

The novelty of the presented manuscript lies in the discovery of 1D bandgaps in these surface-based structures, which has not been presented before, and in providing numerical results that can be used to design an AM lattice structure with a desirable bandgap. Many applications in different industries are expected to exploit the ability of TPMS structures to provide vibration bandgaps. For example, the transport sector could make use of TPMS lattice structures for sound absorption in vehicles, while benefitting from their inherently lightweight nature. Structural frames for precision machines would also benefit from TPMS lattices; they could be used to isolate environmental vibration within certain frequency ranges; for example, those associated with laboratory or workshop equipment.

This paper is structured as follows: Section 2 provides the theoretical background of the finite element method and introduces the TPMS lattice unit cells used in the study. Section 3 presents the method of obtaining the dispersion curves associated with each of the TPMS lattices. Section 4 presents and discusses the dispersion curves of the TPMS lattices. The dependance of the frequency and bandwidth of the bandgaps on the cell size and volume fraction is presented in Sections 4.1 and 4.2, respectively, with the aim of providing a simple tool for designing bandgaps at desired frequencies. Prototype structures are fabricated with additive manufacturing to demonstrate the manufacturability of surface-based lattices; the results are reported on in Section 4.3. Conclusions are provided in Section 5.

2. Mechanical bandgaps in phononic structures

2.1. The lattice unit cells

AM has enabled the design of structures with tailorable mechanical properties using lattice structures. The properties of a lattice are not solely dependent on its constituent material, but also on its cellular geometry, the connectivity of features, unit cell size, number of cell tessellations and volume fraction [1,27].

The lattice unit cells used in this study are the network and matrix phases of the gyroid and diamond surface, as shown in Fig. 1. Network phase cells have one void region and one solid region, both of which retain their connectivity in every part of the structure. Matrix phase lattices have two non-connected void regions separated everywhere by a solid wall or sheet. In addition, matrix phase lattices are known to have higher specific stiffness than their network phase equivalents [26].

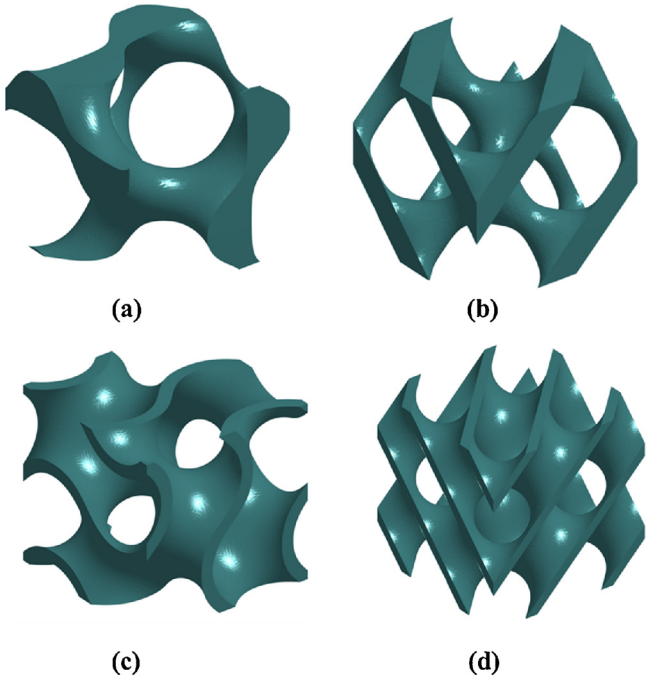

Fig. 1. Representations of the TPMS unit cells used in the study. (a) Network gyroid, (b) network diamond, (c) matrix gyroid, and (d) matrix diamond.

The determination of phonon dispersion curves requires analysis of a single lattice unit cell. The unit cells are designed using software developed at University of Nottingham called the Functional Lattice Package (FLatt Pack) [28]. The volume fraction and size of the cells shown in Fig. 1 is 20% and 15 mm (initial settings), respectively. These values are based on the properties of unit cells that have provided vibration isolation in previous work [1,4].

The geometrical specifications of the unit cells are shown in Table 1. The minimum feature size of the matrix unit cells is the sheet thickness. For network type unit cells, the thickness differs across the unit cell.

Table 1
Geometric specifications of the unit cell used in this study. The parameter t identifies the thickness of the minimum feature in each unit cell.

Unit cell	Unit cell size, L/mm	Volume fraction/%	t/mm	t/L	Schematic
Network gyroid	15	20	3.8	0.25	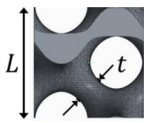
Matrix gyroid	15	20	1.05	0.07	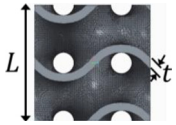
Network diamond	15	20	2.55	0.17	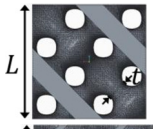
Matrix diamond	15	20	1.05	0.07	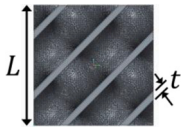

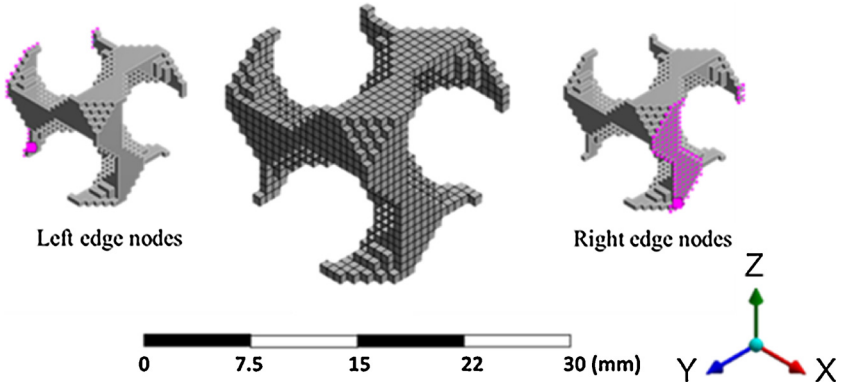

Fig. 2. Hexahedral mesh of a gyroid unit cell used in this work. The highlighted areas illustrate the nodes of the right and left edges of the cells which need to be identified for application of the finite element method.

The parameter t for the network unit cells is, therefore, defined as the thickness in the slimmest regions. Design equations of gyroid and diamond TPMS can be found in the AM work of Maskery et al. [20] and chemistry work of Gandy et al. [29], respectively.

2.2. Finite element method

The finite element method used in this paper relies on Bloch theorem, which governs the displacement of the element nodes. Floquet boundary conditions are used, which simulate an infinite tessellation of the unit cell [30]. The work uses 3D lattice models with three DOF at each node to capture all the possible modes of vibration. This technique is common in the analysis of 1D dispersion characterisation, including the prediction of bandgap formation in elastic mechanical structures [8,18,31,32].

Bandgaps always appear within the boundaries of the first Brillouin zone (BZ) [15,33,34]. The 1D BZ of a square lattice spans from 0 to 2 π/L, where L is the lattice parameter of the unit cell. The propagation of the wave across the 1D BZ can be understood by studying the motion of the wave in a single 3D unit cell. This provides time savings in the analysis of wave propagation in periodic structures.

The motion of a structure without an external driving force can be described as

$$\boldsymbol{M_s}\ddot{\mathbf{q}} + \boldsymbol{K_s}\boldsymbol{q} = \mathbf{0} \tag{1}$$

where $\boldsymbol{M_s}$, $\boldsymbol{K_s}$ and $\boldsymbol{q}$ represent the mass matrix, the stiffness matrix and the displacement vector of the structure of interest, respectively. The effect of damping is not included in this paper, but the reader is referred to the work of Belle et al. [35] for information on the effect of damping on the dispersion curves.

The Bloch theorem for 1D wave propagation without attenuation gives

$$\boldsymbol{q_r} = e^{-ikL}\boldsymbol{q_l}, \tag{2}$$

where $\boldsymbol{q_r}$ and $\boldsymbol{q_l}$ denote the DOFs of the right and left nodes of the 3D unit cell respectively (see Fig. 3) and k is the wave number of a specific wave in the first BZ. The displacement vector $\boldsymbol{q}$ can be projected to a reduced vector $\tilde{\mathbf{d}}$ that denotes the displacement of the nodes in reduced coordinates using the following Bloch's transformation:

$$\boldsymbol{q} = \boldsymbol{T}\tilde{\mathbf{d}},$$
$$\boldsymbol{q} = \begin{bmatrix} \boldsymbol{q_l} \\ \boldsymbol{q_i} \\ \boldsymbol{q_r} \end{bmatrix}, \quad \boldsymbol{T} = \begin{bmatrix} \mathbf{I} & \mathbf{0} \\ \mathbf{I}e^{-ikL} & \mathbf{0} \\ \mathbf{0} & \mathbf{I} \end{bmatrix}, \quad \tilde{\mathbf{d}} = \begin{bmatrix} \boldsymbol{q_l} \\ \boldsymbol{q_i} \end{bmatrix}, \tag{3}$$

where $\boldsymbol{I}$ denotes an identity matrix of proper size and $\boldsymbol{T}$ is a transformation matrix. To obtain the governing equations in the new reduced coordinates, Bloch's transformation of Eq. (3) can be substituted into Eq. (1) and multiplied by $\boldsymbol{T^T}$ to ensure equilibrium in both sets of coordinates. This gives

$$\tilde{\mathbf{D}} = \boldsymbol{T^T}\boldsymbol{D}\boldsymbol{T} \quad \boldsymbol{D} \equiv \boldsymbol{K} - \omega^2\boldsymbol{M} \tag{4}$$

where $\boldsymbol{T^T}$ is the Hermitian transpose of the matrix $\boldsymbol{T}$ and $\boldsymbol{D}$ is the dynamic stiffness matrix that contains the mass matrix $\boldsymbol{M}$ and the stiffness matrix $\boldsymbol{K}$ [30]. The eigenvalue problem is then obtained in the form

$$\tilde{\mathbf{D}}\tilde{\mathbf{d}} = \mathbf{0} \tag{5}$$

By solving Eq. (5), frequency modes for each wave vector in the first BZ can be obtained.

3. Methodology

3.1. Calculation of the dispersion curve

Voxel models of the TPMS unit cells are assigned the properties of selectively laser sintered Nylon-12, which has a density of 0.95 g/cm^3 and a Young's modulus of 1500 MPa [36]. The voxelised network gyroid cell is shown in Fig. 2, in which the leftmost and rightmost nodes are highlighted. A finite element method is used for modelling the structure and Periodic Structure Theory (PST) is used for correlating the displacements [18,19]. The modelling assumes an infinite tessellation of lattice cells along the $x-$ direction.

The mass and stiffness matrices of the unit cells are rearranged with the help of the nodes numbering obtained from a commercial finite element package. The mass and stiffness matrices are then arranged in the form shown in Eq. (3). The generalised eigenvalue problem of Equation (5) is constructed. The frequency eigenvalue problems are solved for 100 equally spaced wave numbers spanning the first BZ of the TPMS unit cells. All wavebands below 15 kHz in each lattice were included in the analyses.

3.2. Bandgap tuning method

The properties of lattice structures that can be tuned to potentially induce a phononic bandgap include cell size, volume fraction and cell geometry. Here, the four unit cells identified in Section 2.1 will be analysed first, with the most promising candidate for bandgap development then being chosen for bandgap tuning. The characteristic wavebands for the initial settings of the chosen cell found under 15 kHz are examined under different volume fractions and cell sizes. The range of volume fractions used in this study extends from 20% to 40%, while the examined cell sizes are of 15 mm, 20 mm, 25 mm, 30 mm and 40 mm.

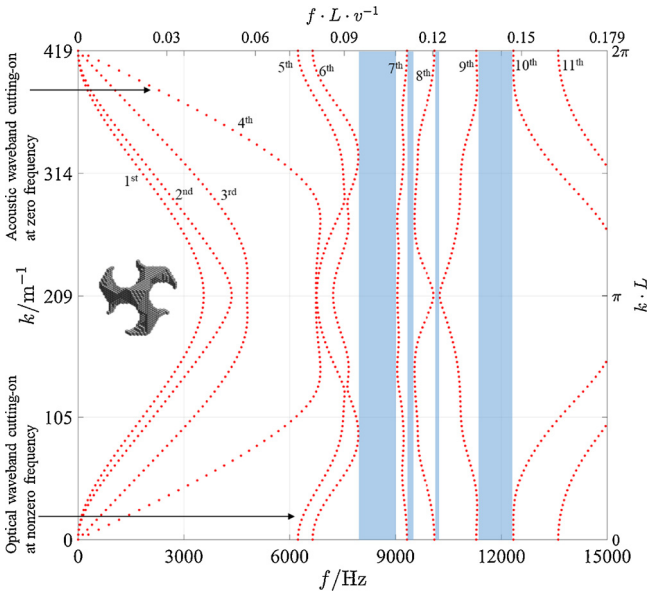

Fig. 3. Phonon dispersion curves for the network gyroid lattice with 15 mm cell size and 20% volume fraction as modelled with the properties of AM Nylon-12. Shaded zones represent the bandgaps. Wavebands are numbered from the 1st to the 11th waveband. The top axis shows the frequency f normalised to the lattice unit cell size L and the speed of the wave v in the material, while the right axis shows the wavenumber normalised to the lattice unit cell size.

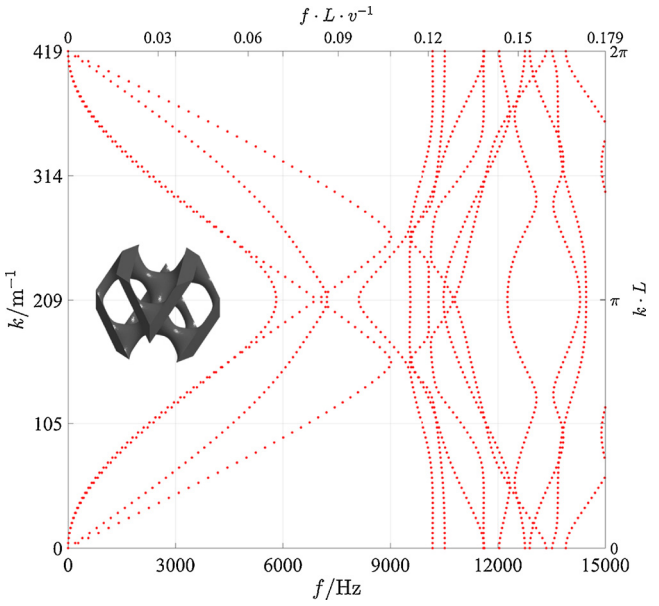

Fig. 4. Phonon dispersion curves for the network diamond lattice with 15 mm cell size and 20% volume fraction.

4. Results and discussion

The mass and stiffness matrices on which the phonon dispersion curves depend were found to have converged with respect to the mesh density. The bandgap dispersion curves for the network gyroid lattice, shown in Fig. 3, show a total of four bandgaps in the sub-15 kHz region. The broadest is formed between the 6th and 7th wavebands, is 1047 Hz wide and starts from 7905 Hz A bandgap of similar width spans 978 Hz from 11,349 Hz to 12,327 Hz and is formed by the 9th and 10th wavebands. A bandgap narrower in width than the previous two appears in the range of 9340 Hz to 9506 Hz, and another one appears in the range of 10,134 Hz to 10,238 Hz.

The scattering of the mechanical waves in a structure relies on the impedance mismatch between two adjacent geometrical features [37]. As shown in Figs. 3 and 4, the network gyroid lattice possesses phononic bandgaps below 15 kHz while the network diamond lattice does not. This can be explained by considering the differing internal geometries of the respective cells. As a wave travels from a thicker to a thinner solid region of the cell, or from the solid phase to the void phase, it is partially reflected, owing to the change in local impedance. This process is repeated for each reflected wave, giving rise to complex dispersion curves such as those in Figs. 3 and 4.

The lowest frequency bandgap is usually formed by one acoustic waveband (a waveband cutting-on at 0 Hz) and one optical waveband (a waveband cutting-on at nonzero frequency) [30]. Although Bragg bandgaps can also be formed by two optical wavebands, which is the case of all the bandgaps in this paper, it is impossible for a Bragg bandgap to be formed before the cut-off frequency of acoustic wavebands. We compare the ability of the network diamond and the matrix diamond lattices to form bandgaps by examining the cut-off frequency of their acoustic wavebands. As can be seen in Figs. 4 and 6, respectively, the acoustic wavebands cut-off at a higher frequency in the matrix diamond cell (around 14,000 Hz) while they cut off at a much lower frequency (around 9000 Hz) in the network diamond cell. The network diamond lattice also showed a larger number of wavebands within the tested frequency region. However, similar to its matrix counterpart, the network diamond cell did not possess bandgaps within the examined frequency range.

Similar behaviour is observed by the network gyroid and the matrix gyroid cells; the cut-off frequency of acoustic wavebands of the network gyroid cell is around 7000 Hz while the corresponding frequency in the matrix gyroid cell is around 9600 Hz. The matrix gyroid formed a bandgap spanning from 12,952 Hz to 13,220 Hz. This bandgap is higher in terms of the starting frequency and narrower in terms of width than the lowest frequency bandgap observed in the gyroid network cell. In addition, matrix type lattices have almost constant wall thickness across the inner parts of the cell. This suggests that matrix cells would have reduced capacity to hinder wave propagation from one end of the cell to the other than in the network type lattices. This is because wave reflection, which is the mechanism by which Bragg induced bandgaps are formed, is expected to be higher when there is a large difference in densities; or large difference in wall thickness.

The dispersion curves of the matrix lattices support the claim presented by Kapfer et al. [26] in that matrix type lattices have higher stiffness than network type lattices. The examined lattices are of identical volume fraction and cell size and, therefore, identical mass. Thus, the natural frequency of a matrix type lattice is higher than its corresponding network counterparts. In wave reflection by Bragg scattering, the bandgap does not appear at frequencies lower than the natural frequency of the structure. Thus, the high natural frequency of matrix gyroid lattice, as can be seen from Fig. 7, prohibits the opening of bandgaps at lower frequencies than the network gyroid lattice. This is seen in Fig. 3 and 5, where one bandgap appears in the matrix gyroid dispersion curves, while several appear within the same frequency range using the network gyroid lattice. The reader is referred elsewhere [23] for more information on matrix and network type TPMS lattices.

4.1. Tuning lattice bandgaps through cell size selection

The network gyroid lattice represents a suitable candidate to examine the control of bandgaps, because we have established that it supports multiple bandgaps at a practical cell size and volume fraction, as demonstrated in Section 4. The absolute bandgaps frequencies arising from the network gyroid lattice with cell sizes of 15 mm, 20 mm, 25 mm, 30 mm and 40 mm, at constant volume fraction of 20%, are calculated. Fig. 8 shows the dependency of the absolute bandgaps frequencies on the cell size of Nylon-12. The bandgap with the largest bandwidth was seen for the 15 mm cell, where the bandgap spanned

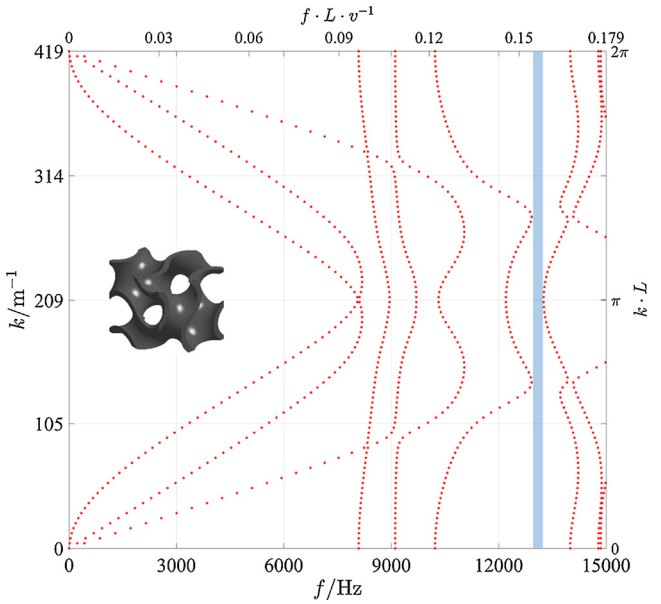

Fig. 5. Phonon dispersion curves for matrix gyroid lattice with 15 mm cell size and 20% volume fraction.

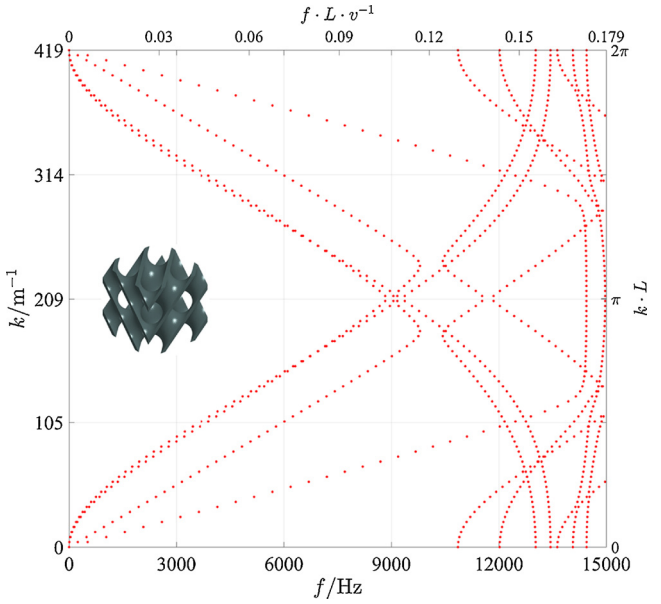

Fig. 6. Phonon dispersion curves for matrix diamond lattice with 15 mm cell size and 20% volume fraction.

approximately 1048 Hz from 7905 Hz to 8953 Hz.

Of the examined network gyroid cell sizes, the 40 mm lattice showed a bandgap of the lowest frequency. This bandgap is formed between wavebands 6 and 7. The starting frequency of this bandgap is around 60% lower than the corresponding band gap in the 15 mm cell.

Since the bandgap analyses assumes infinite tessellations of the lattice cell along the x -direction, we have chosen settings of nine unit cells to examine the harmonic response of this network gyroid cell. According to Chen et al. [38], any number of unit cells higher than seven is enough to spot the bandgap with harmonic response analysis; this is to determine whether a wave would propagate or not. The number of unit cells which we chose, nine, is an arbitrary one that fits the criteria of Chen et al. The analyses were carried on the 40 mm network gyroid cell structure by exciting one of its faces with an oscillating load. The load was 1 N and was applied in the $x-$ direction to all the leftmost nodes in the structure. The movement of the rightmost nodes in $x-$, $y-$ and $z-$ directions are depicted. From Fig. 9, it can be seen that the bandgaps of 40 mm network gyroid, presented in Fig. 8, correspond to attenuation in the harmonic response diagram. The finite length of the structure can be the cause of resonances in the frequency regions of some bandgaps. From our previous work [1,4], we assert that 40 mm cells are less stiff than 15 mm cells of similar configurations due to higher dominance of bending behaviour in larger cells. This lower stiffness, of the 40 mm gyroid cell compared to the 15 mm cell, is translated into lower bandgap frequency.

4.2. Tuning lattice bandgaps through volume fraction selection

Phonon dispersion curves for the network gyroid lattices with volume fractions of 20%, 25%, 30%, 35% and 40% were simulated at a constant cell size of 15 mm. The unit cell information, including the t/L ratio for the network gyroid unit cells at different volume fraction, are shown in Table 2.

The phonon dispersion curves of these lattices are presented in Figs. 3 and 10. Fig. 11 shows the dependence of the bandgaps on the volume fraction of the 15 mm cell.

The width of the bandgap between the 9th and the 10th wavebands was the largest at a volume fraction of 25% and spanned a frequency range of around 1900 Hz. Increasing the volume fraction above this value reduced the width of this bandgap. In addition, the starting frequencies of all bandgaps increased with the increase in volume fraction, except between wavebands 9 and 10, where the starting frequency showed a reduction of approximately 1% over that of 20% volume fraction network gyroid.

The bandgap between the 8th and 9th wavebands disappeared when the volume fraction went from 20% to 25%, but it returned when the volume fraction was 30%, 35% and 40%. Similar behaviour is observed by the bandgap of wavebands 6 and 7; this one does not appear in the 35% and 40% volume fraction dispersion curves. Thus, the bandgap formed by the 9th and the 10th wavebands and the bandgap formed by the 7th and the 8th wavebands are the only bandgaps that sustained the variation of the volume fraction and the cell size.

The network gyroid cell with 40% volume fraction shows a bandgap between wavebands 9 and 10 which appears at a starting frequency 45% greater than that of the 20% volume fraction cell. These results indicate a means to control the frequency and width of phononic bandgaps in lattice structures by controlling their volume fraction.

Similar to the harmonic analyses carried on the 40 mm network gyroid cell structure, harmonic response analyses were carried on the 40% volume fraction network gyroid cell, with nine tessellations along the $x-$ direction, by exciting one of its faces with an oscillating load. The load was 1 N and was applied in the $x-$ direction to all the leftmost nodes in the structure. The movement of the rightmost nodes in $x-$, $y-$ and $z-$ directions are depicted. From Fig. 12, it can be seen that the bandgaps present in 40% volume fraction cell's dispersion curve, which are shown in Fig. 11(d), correspond to vibration attenuation in the harmonic response diagram. In addition, it is observed that the TPMS structure has the ability to provide attenuation at non-bandgap frequencies. The results suggest that development of wide bandgaps is possible with the network gyroid lattice. The starting frequency of the bandgaps can be reduced for specific applications by reducing the volume fraction of the lattice.

The bandgap behaviour of AM surface-based lattice structures has not received much attention. Of relevance to our investigation is the work of Matlack et al. [18], who used internal resonators lattices, allowing the development of bandgaps with starting frequencies of 3000 Hz–4000 Hz. Our work shows that TPMS structures have the ability to open up bandgaps at similar starting frequencies with the potential to go even lower by choosing an appropriate cell size and volume fraction.

Using multi-material unit cells can result in large differences in

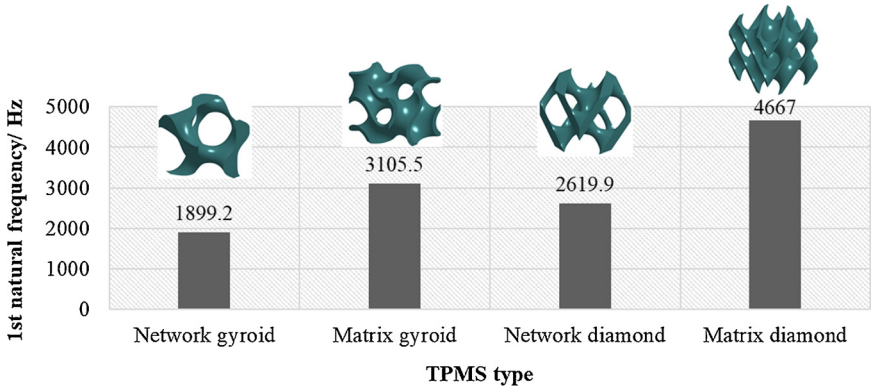

Fig. 7. 1st natural frequency of the same resonance mode for four types of TPMS lattices unit cells as modelled in FE with the initial settings of 15 mm cell size and 20% volume fraction. A matrix TPMS has higher 1st natural frequency than its corresponding network counterpart.

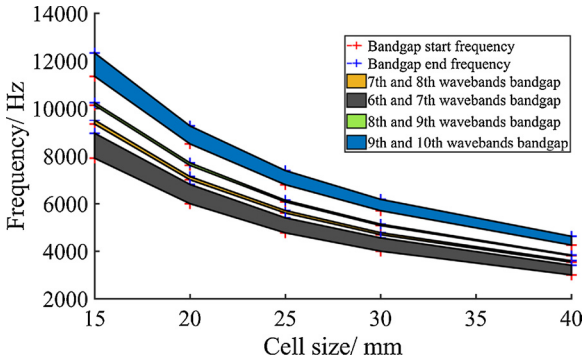

Fig. 8. Dependence of network gyroid bandgaps on the cell size.

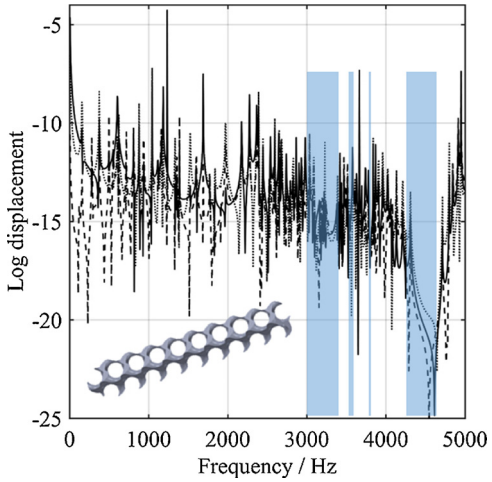

Fig. 9. Harmonic response of 40 mm network gyroid cell with nine tessellations along the $x-$ direction in longitudinal (solid line), $y-$ transverse (dashed line), and $z-$ transverse (dotted line) directions.

Table 2
Network gyroid unit cells specification at different volume fractions.

Unit cell size L/mm	Volume fraction/ %	t/mm	t/L	Schematic
15	20	3.8	0.25	
15	25	4.35	0.29	
15	30	4.9	0.33	
15	40	5.95	0.4	

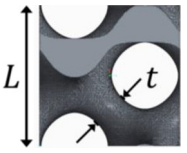

impedance and ultimately a wider bandgap than those reported in this work; Ampatzidis et al. [8] presented a structure of Nylon-12 glued to a composite panel that provided a 1D bandgap. The normalised bandgap frequency of their structure was from 0.24 to 0.27. In comparison to the first bandgap of 20% volume fraction gyroid examined in this work, the structure of Ampatzidis et al. is higher by 160% in terms of the starting normalised bandgap frequency and wider by 50%. Lucklum et al. [12] presented a bandgap of normalised frequency between 0.15 to 0.25. In this work, the normalised frequency of the first bandgap formed by the 20% gyroid unit cell is from 0.09 to 0.11. This bandgap is lower by 40% in terms of the starting frequency and narrower by 90% in terms of width than the bandgap presented by Lucklum et al.

However, single material designs are more easily made with additive manufacturing than multi-material designs. Single material structures are reported by Kruisove et al. [13] who presented four bandgap structures of lattice unit cell sizes as low as 200. Kruisove et al. used an extrusion based additive manufacturing technology to manufacture these strut-based micro lattices with bandgaps from 3 MHz. The closest bandgap structure, reported by Kruisova et al., to the bandgap structures in this work, in terms of equal lattice constants in 3D is their "SS model". The SS model had dimensions of 308 μm, 219 μm and 261 μm in $x-$, $y-$, and $z-$ directions with a starting bandgap frequency of 9 MHz. Normalising this bandgap with the average lattice constant of 262 μm and the speed of the wave in SiC material to compare with the network gyroid bandgap gives a normalised starting bandgap frequency of 0.26. This starting bandgap frequency is higher by 180% than the normalised starting frequency of the first bandgap formed by 20% volume fraction gyroid reported here.

4.3. Fabrication with additive manufacturing

Network gyroid prototype samples were fabricated on a selective laser sintering (SLS) system using a 21 W laser of a scan speed and hatch spacing of 2500 mm·s^{-1} and 0.25 mm, respectively. The nominal spot size of the laser is 0.3 mm and the layer thickness is 0.1 mm. Nylon-12 material is used to fill a 1320 mm × 1067 mm × 2204 mm powder bed at a temperature of 173 °C.

The theoretical size threshold below which the network gyroid would be fabricated with major defects (i.e. deviations from the nominal or CAD geometry) is determined by the accuracy of the SLS system and the geometry of the network gyroid cell. The SLS properties affecting precision include the laser spot size, layer thickness, powder size, and laser scanning strategy. The network gyroid cell properties are the cell size L, and the volume fraction VF, which together determine the minimum feature thickness t. Features of sizes close to the laser spot size and below 0.8 mm are expected to be fabricated with significant losses in mechanical properties; this is because higher amount of unmelted or partially melted powder exists in features of sizes below

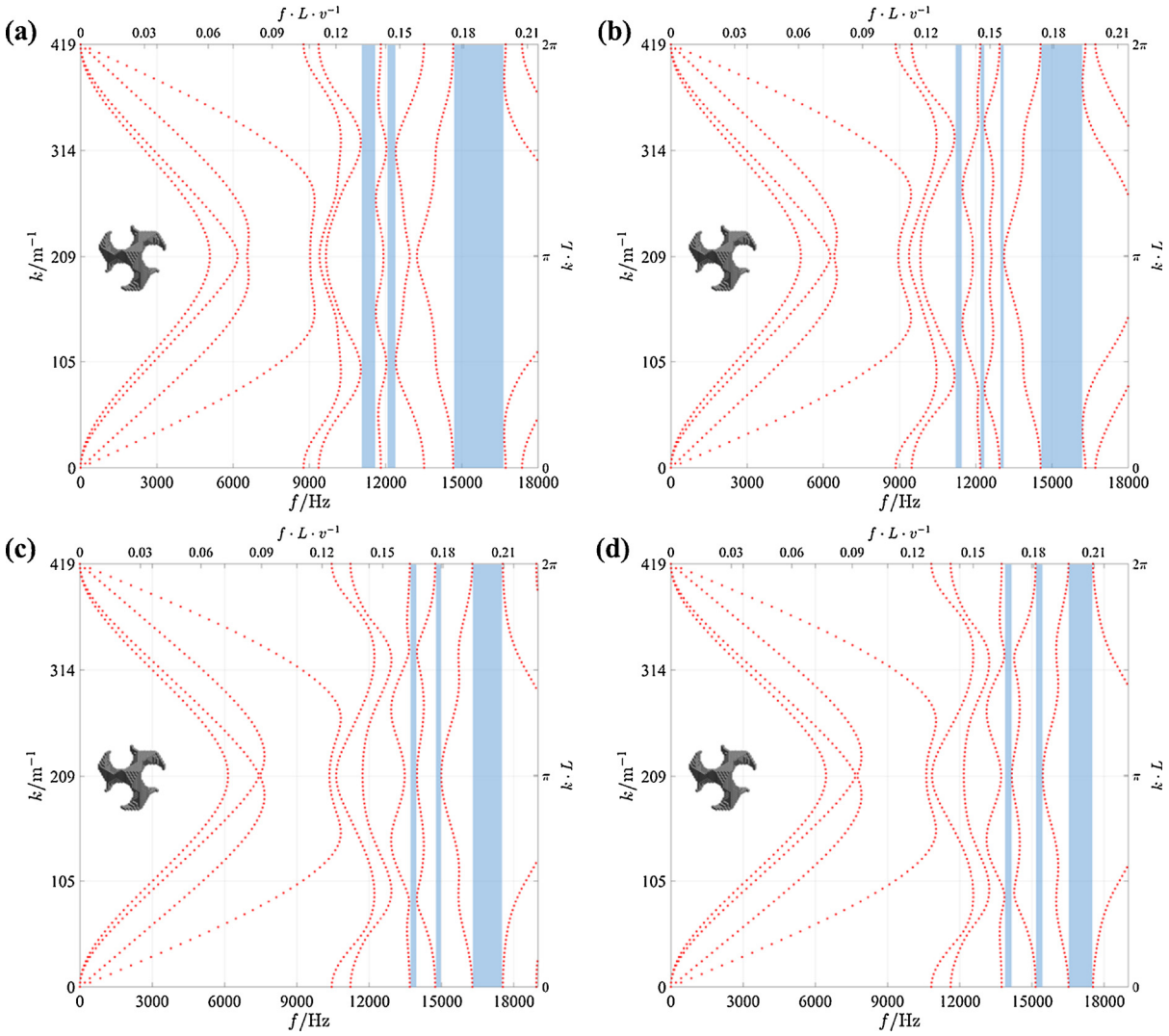

Fig. 10. Phonon dispersion curves for the network gyroid lattice with 15 mm cell size at different volume fractions of (a) 25%, (b) 30%, (c) 35%, and (d) 40%.

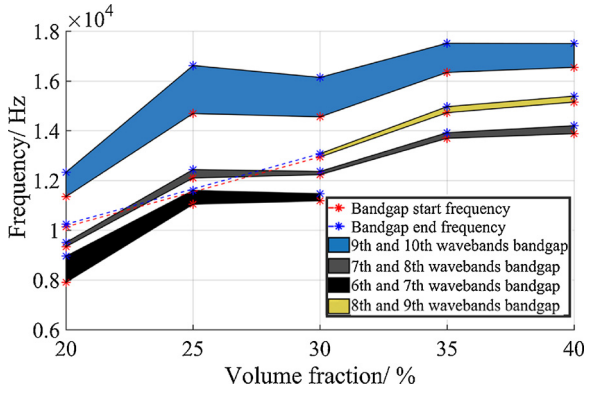

Fig. 11. Dependence of network gyroid bandgaps on the volume faction.

0.8 mm, in comparison to thicker features [39].

Fig. 13 shows the dependency of t on the volume fraction and cell size of the unit cell. The lower SLS manufacturing limit is set to 0.8 mm to ensure minimal loss of mechanical properties [39]. The t/L ratio was obtained from CAD models at volume fractions between 0% to 40% using a step of 5%. The relationship between t, L and VF as obtained by plotting the data from the CAD models is

$$t = L \times (0.0075 \times VF + 0.1) \quad (6)$$

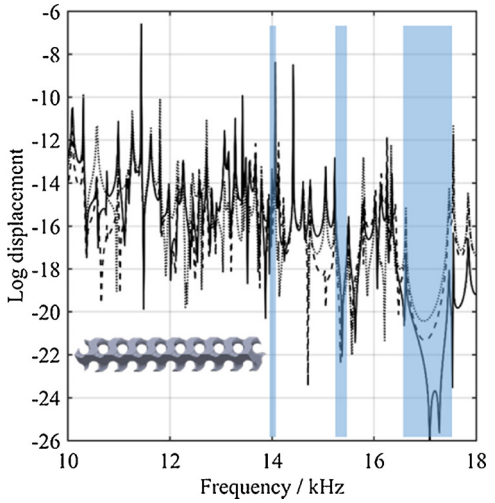

Fig. 12. Harmonic response of 40% volume fraction gyroid cell with nine tessellations along the $x-$ direction in longitudinal (solid line), $y-$ transverse (dashed line), and $z-$ transverse (dotted line) directions.

By substituting $t = 0.8$ mm, and $VF = 0.2$ while solving for L, we theoretically obtain the lowest achievable cell size at 20% volume

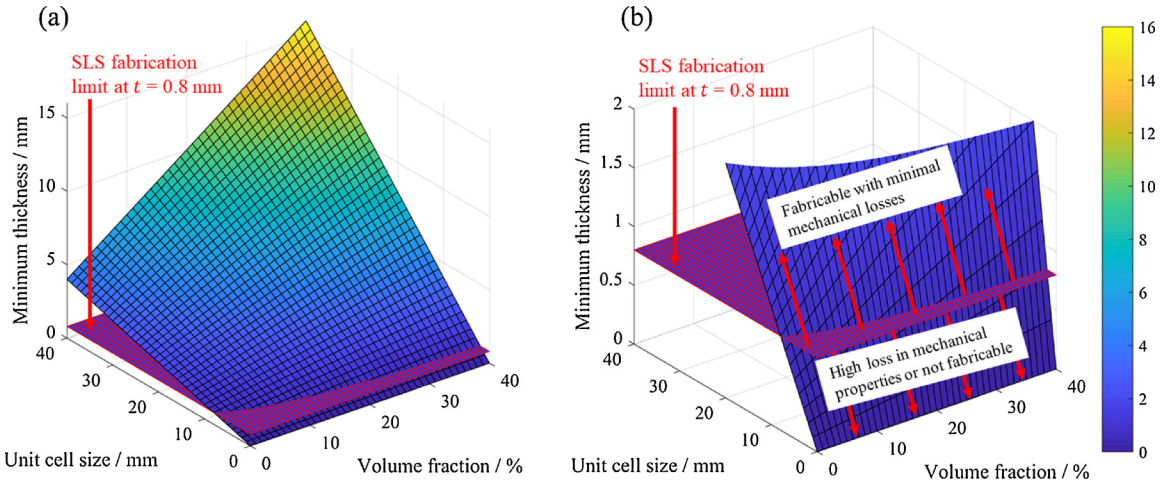

Fig. 13. (a) Minimum thickness t of network gyroid unit lattice at different volume fractions and unit cell sizes L, and (b) zoomed in view with labeled fabricable and not fabricable design spaces.

fraction which is 7.8 mm. More generally, Eq. (6) can be used to determine the minimum value of VF or L for the gyroid lattice produced once the other is specified.

SLS is employed to fabricate 20% volume fraction lattices of four tessellations along the $x-$ axis, with cell sizes of 15 mm, 25 mm and 40 mm. These will be referred to as lattice 1, 2 and 3, respectively. Two copies of each lattice were fabricated and they are shown in Fig. 14. Table 3 shows the nominal and average length and mass properties. The nominal values were extracted from the CAD models.

The measured values are measured using a vernier caliper for length and a mass balance for mass. Each measurement was repeated four times and the standard error of the measurements are shown alongside the mean properties in Table 3. The measured volume fraction is calculated as the ratio between the measured mass and the mass of a solid structure of dimensions identical to the measured lattice assuming a 950 kg·m^{-3} density (that of SLS Nylon 12) [36].

The differences between the properties of copies of the lattice structures were insignificant, as they all fell within the standard error of the measurements of each property. Comparing the measured properties to the nominal properties, the mass of the fabricated lattices was lower by 4.9%, 2.1%, and 0.3% in lattice 1, lattice 2, and lattice 3, respectively. The difference in the mass translated into a reduction of 10% and 2.4% from the nominal volume fraction of lattice 1 and lattice 2, respectively. The length measurements showed a 3.2% decrease in the t values of lattice 1. For lattice 2, the deviation from the nominal t value was lower, 1.52%. The measured cell size showed deviations of

Table 3
Nominal and measured properties of 4 × 1 × 1 network gyroid lattice fabricated with SLS. The standard error is provided for each measured property.

Property	Lattice 1	Lattice 2	Lattice 3
Nominal L / mm	15	25	40
Measured L / mm	15.26 ± 0.03	25.03 ± 0.02	39 .98 ± 0.03
Nominal mass / g	2.56	11.88	48.712
Measured mass / g	2.43473 ± 4 ×10^{-5}	11.6314 ± 5 ×10^{-5}	48.56755 ± 2 ×10^{-5}
Nominal t / mm	3.75	6.25	10
Measured t / mm	3.63 ± 0.04	6.16 ± 0.03	10.01 ± 0.03
Nominal volume fraction / %	20	20	20
Measured volume fraction / %	17.99 ± 0.06	19.52 ± 0.02	19.99 ± 0.02

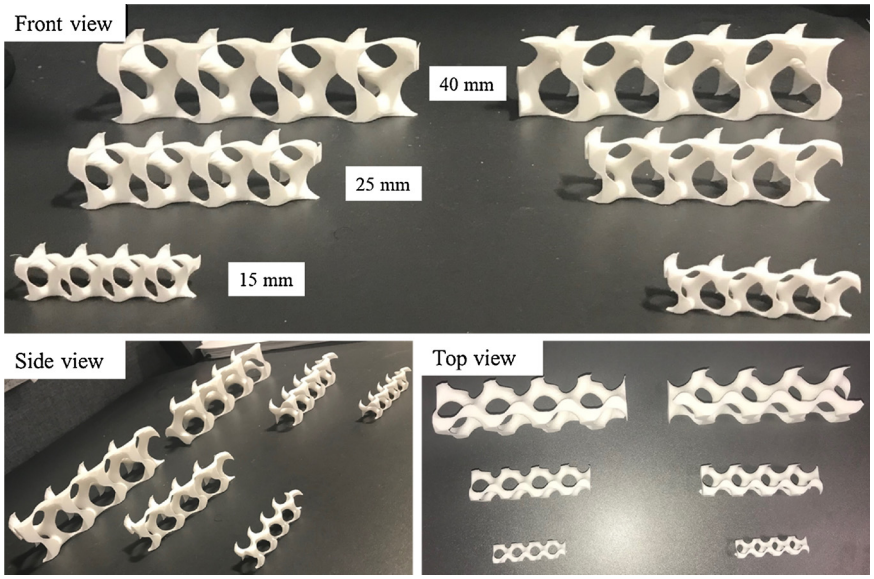

Fig. 14. Prototype samples of network gyroid lattice of 15 mm, 25 mm, and 40 mm unit cell sizes, all in 4 × 1 × 1 tessellations. The size of the single unit cell is indicated in the front view. Fabrication is made with SLS using Nylon-12 powder.

1.8%, and 0.11% from the corresponding nominal values of lattice 1, and lattice 2, respectively. However, the measured deviations in the minimum thickness, cell size and volume fraction from the nominal values of lattice 3 are insignificant as they are smaller than the standard error of their measurements. All length deviations are below the laser spot size in SLS.

Future advances in the accuracy and minimum feature sizes of SLS systems are expected to reduce the gap between the nominal and fabricated lattices. These improvements may also push the theoretical cell size limit for gyroid lattices below the fabrication limits which are set in Fig. 13, for example, below 7.8 mm for 20% volume fraction gyroid cells. This will provide an opportunity to open bandgaps at higher frequencies by manufacturing unit cells of lower cell sizes.

5. Conclusions

We demonstrated that TPMS lattice structures can induce mechanical bandgap behaviour which can be tailored for vibration isolation purposes. The novelty of the presented work lies in predicting the 1D bandgaps of beam-like surface-based lattices, which have not been studied before. Our analysis showed that:

- At reasonable cell sizes and volume fractions for AM capabilities, the network gyroid and the matrix gyroid lattices have bandgaps, while other examined lattice types do not.
- Changing the lattice cell size and volume fraction of surface-based lattices can alter the width of a pre-existing bandgap, the starting frequency, or both. In addition, the potential to open up bandgaps that did not exist previously between two wavebands was demonstrated.
- The network gyroid and the matrix gyroid TPMS lattices have several bandgaps under 15 kHz when their volume fraction is 20% and cell size is 15 mm.
- Bandgaps at frequency regions as low as 3000 Hz are demonstrated to be achievable using a cell size of 40 mm and 20% volume fraction.

Fabrication of prototype lattice structures was done using SLS system which fabricated $4 \times 1 \times 1$ lattices of cell sizes of 15 mm, 25 mm, and 40 mm. The SLS system fabricated the lattices with a maximum deviation of 1.8% and 10% from the nominal cell sizes and volume fractions, respectively. The measured minimum feature t showed a maximum difference of 3.2% from the nominal value. All the differences between measured and nominal values are below the laser spot size in SLS which is 0.3 mm.

Introduced here are new design factors for tuning bandgaps of phononic structures which are realised by the nature of TPMS lattices and the manufacturing freedom of AM. The designer of lattice structures can now use these results to design and fabricate structures with AM that exhibit inherent vibrational isolation properties for the use in different engineering applications. More work, including the control of more TPMS parameters for tuning mechanical bandgaps, will follow. Additional work for opening bandgaps in more propagation directions and at lower frequencies using AM lattice structures is also in progress.

Acknowledgments

This work was supported by the Engineering and Physical Sciences Research Council [grant number EP/M008983/1]. The authors would like to thank Theofanis Ampatzidis and Joseph White (University of Nottingham) for helping with this work.

References

[1] W.P. Syam, W. Jianwei, B. Zhao, I. Maskery, W. Elmadih, R.K. Leach, Design and analysis of strut-based lattice structures for vibration isolation, Precis. Eng. (2017).
[2] W. Elmadih, M. Nefzi, E. Bruice, Environmental isolation, in: R.K. Leach, S. Smith (Eds.), Basics Precis. Eng. 2018, pp. 565–600.
[3] T.L. Schmitz, K.S. Smith, Mechanical Vibrations: Modeling and Measurement, Springer, New York, 2011.
[4] W. Elmadih, W.P. Syam, I. Maskery, R.K. Leach, Additively manufactured lattice structures for precision engineering applications, 32nd Annu. Meet. Am. Soc. Precis. Eng. (2018) In Press.
[5] X. Wang, P. Zhang, S. Ludwick, E. Belski, A.C. To, Natural frequency optimization of 3D printed variable-density honeycomb structure via a homogenization-based approach, Addit. Manuf. (2017).
[6] Z. Liu, C.T. Chan, P. Sheng, Three-component elastic wave band-gap material, Phys. Rev. B - Condens. Matter Mater. Phys. 65 (2002) 1651161–1651166.
[7] M. Kushwaha, Classical band structures of periodic elastic composites, Int. J. Mod. Phys. B. 10 (1996) 977–1094.
[8] T. Ampatzidis, R.K. Leach, C.J. Tuck, D. Chronopoulos, Band gap behaviour of optimal composite structures with additive manufacturing inclusions, Compos. Part B (2018).
[9] D.J. Richards, D. Pines, Passive reduction of gear mesh vibration using a periodic drive shaft, J. Sound Vib. 2 (2003) 317–342.
[10] J.S. Sigmund, O. Jensen, Systematic design of phononic band-gap materials and structures by topology optimization, Math. Phys. Eng. Sci. 1806 (2003) 1001–1019.
[11] L. Diaz, A.R. Haddow, A.G. Ma, Design of band-gap grid structures, Struct. Multidiscipl. Optim. 29 (2005) 418–431.
[12] F. Lucklum, M.J. Vellekoop, Design and fabrication challenges for millimeter-scale three-dimensional phononic crystals, Crystals 7 (2017) 348–361.
[13] A. Kruisová, M. Ševčík, H. Seiner, P. Sedlák, B. Román-Manso, P. Miranzo, M. Belmonte, M. Landa, Ultrasonic bandgaps in 3D-printed periodic ceramic microlattices, Ultrasonics 82 (2018) 91–100.
[14] M. Wormser, F. Wein, M. Stingl, C. Körner, Design and additive manufacturing of 3D phononic band gap structures based on gradient based optimization, Materials (Basel) 10 (2017) 1125.
[15] F. Maurin, C. Claeys, E. Deckers, W. Desmet, Probability that a band-gap extremum is located on the irreducible Brillouin-zone contour for the 17 different plane crystallographic lattices, Int. J. Solids Struct. (2017).
[16] M. Ruzzene, F. Scarpa, F. Soranna, Wave beaming effects in two-dimensional cellular structures, Smart Mater. Struct. 12 (2003) 363–372.
[17] D.W. Abueidda, I. Jasiuk, N.A. Sobh, Acoustic band gaps and elastic stiffness of PMMA cellular solids based on triply periodic minimal surfaces, Mater. Des. 145 (2018) 20–27.
[18] K.H. Matlack, A. Bauhofer, S. Krödel, A. Palermo, C. Daraio, Composite 3D-printed Metastructures for Low Frequency and Broadband Vibration Absorption, (2015), pp. 1–5.
[19] J. Li, Y. Wang, C. Zhang, Finite element method for analysis of band structures of phononic crystal slabs with archimedean-like tilings, AIP Conf. Proc. (2009), pp. 1548–1551.
[20] I. Maskery, L. Sturm, A.O. Aremu, A. Panesar, C.B. Williams, C.J. Tuck, R.D. Wildman, I.A. Ashcroft, Insights into the mechanical properties of several triply periodic minimal surface lattice structures made by polymer additive manufacturing, Polymer (Guildf) (2017) 1–10.
[21] A. Panesar, M. Abdi, D. Hickman, I. Ashcroft, Strategies for functionally graded lattice structures derived using topology optimisation for additive manufacturing, Addit. Manuf. 19 (2018) 81–94.
[22] O. Al-Ketan, R. Rowshan, R.K. Abu Al-Rub, Topology-mechanical property relationship of 3D printed strut, skeletal, and sheet based periodic metallic cellular materials, Addit. Manuf. 19 (2018) 167–183.
[23] I. Maskery, N.T. Aboulkhair, A.O. Aremu, C.J. Tuck, I.A. Ashcroft, Compressive failure modes and energy absorption in additively manufactured double gyroid lattices, Addit. Manuf. 16 (2017) 24–29.
[24] A.Y. Hussein, The Development of Lightweight Cellular Structures for Metal Additive Manufacturing, (2013), p. 228.
[25] S.N. Khaderi, V.S. Deshpande, N.A. Fleck, The stiffness and strength of the gyroid lattice, Int. J. Solids Struct. 51 (2014) 3866–3877.
[26] S.C. Kapfer, S.T. Hyde, K. Mecke, C.H. Arns, G.E. Schröder-Turk, Minimal surface scaffold designs for tissue engineering, Biomaterials 32 (2011) 6875–6882.
[27] O. Rehme, Cellular Design for Laser Freeform Fabrication, Gottingen (2010).
[28] Added Scientific, Software and Modelling, (2018) (Accessed April 24, 2018), http://addedscientific.com/resources/software-and-modelling.
[29] P.J. Gandy, D. Cvijović, A.L. Mackay, J. Klinowski, Exact computation of the triply periodic D (`diamond') minimal surface, Chem. Phys. Lett. 314 (1999) 543–551.
[30] A.S. Phani, Elastodynamics of lattice materials, in: A.S. Phani, M.I. Hussein (Eds.), Dyn. Lattice Mater. John Wiley and Sons, 2017, pp. 53–59.
[31] A. Khelif, F.L. Hsiao, A. Choujaa, S. Benchabane, V. Laude, Octave omnidirectional band gap in a three-dimensional phononic crystal, IEEE Trans. Ultrason. Ferroelectr. Freq. Control 57 (2010) 1621–1625.
[32] F.C. Hsu, C.I. Lee, J.C. Hsu, T.C. Huang, C.H. Wang, P. Chang, Acoustic band gaps in phononic crystal strip waveguides, Appl. Phys. Lett. 96 (2010) 3–6.
[33] N. Ashcroft, N. Mermin, Solid State Physics, Holt, Rinhert and Winston (1976).
[34] L. Brillouin, Wave Propagation in Periodic Structures, 2nd editio, Dover Publications, 1953.
[35] L. Van Belle, C. Claeys, E. Deckers, W. Desmet, On the impact of damping on the dispersion curves of a locally resonant metamaterial: modelling and experimental validation, J. Sound Vib. 409 (2017) 1–23.
[36] P.A. Materialise, 12 (SLS): Datasheet, (2018) (Accessed January 31, 2018), http://www.materialise.com/en/manufacturing/materials/pa-12-sls.
[37] S. Zhuang, G. Ravichandran, D.E. Grady, An experimental investigation of shock wave propagation in periodically layered composites, J. Mech. Phys. Solids 51 (2003) 245–265.
[38] Y. Chen, H. Yao, L. Wang, Acoustic band gaps of three-dimensional periodic polymer cellular solids with cubic symmetry, J. Appl. Phys. 114 (2013).
[39] D. Tasch, A. Mad, R. Stadlbauer, M. Schagerl, Thickness dependency of mechanical properties of laser-sintered polyamide lightweight structures, Addit. Manuf. 23 (2018) 25–33.